EPJ D
Atomic, Molecular, Optical and Plasma Physics
EPJ.org
your physics journal

Eur. Phys. J. D (2016) 70: 178 DOI: 10.1140/epjd/e2016-70179-4

# Stopping and straggling of H and He in ZnO

Raul C. Fadanelli, Chiara D. Nascimento, Claudia C. Montanari, Julio C. Aguiar, Dario Mitnik, Andrzej Turos, Elzbieta Guziewicz and Moni Behar

edp sciences
Società Italiana di Fisica
Springer

Eur. Phys. J. D (2016) 70: 178
DOI: 10.1140/epjd/e2016-70179-4

THE EUROPEAN PHYSICAL JOURNAL D

Regular Article

# Stopping and straggling of H and He in ZnO

Raul C. Fadanelli[1], Chiara D. Nascimento[1], Claudia C. Montanari[2,a], Julio C. Aguiar[3], Dario Mitnik[2], Andrzej Turos[4,5], Elzbieta Guziewicz[6], and Moni Behar[1]

[1] Laboratorio de Implantação Iônica, Instituto de Física, Universidade Federal do Rio Grande do Sul, Av. Bento Goncalves 9500, 91501-970 Porto Alegre, Brazil
[2] Instituto de Astronomía y Física del Espacio (CONICET-UBA), and Departamento de Física, Facultad de Ciencias Exactas y Naturales, Universidad de Buenos Aires, casilla de correo 67, Sucursal 28, C1428EGA Buenos Aires, Argentina
[3] Autoridad Regulatoria Nuclear, Av. Libertador 8250, C1429BNP Buenos Aires, Argentina
[4] Institute of Electronic Materials Technology, Wólczyńska 133, 01-919 Warsaw, Poland
[5] National Centre for Nuclear Research, Soltana 7, 04-500 Otwock, Poland
[6] Institute of Physics, Polish Academy of Sciences, Al. Lotników 32/46, 02-668 Warsaw, Poland

Received 8 March 2016 / Received in final form 4 May 2016
Published online 1 September 2016 – © EDP Sciences, Società Italiana di Fisica, Springer-Verlag 2016

**Abstract.** We present experimental and theoretical values for the energy loss of H and He ions in Zinc oxide, in mean value (stopping per unit path length) and mean square value (energy loss straggling). The measurements were carried out using the Rutherford Backscattering technique for (300–2000) keV H ions and (300–5000) keV He ions. Present experimental data are the first set of stopping and straggling values in this oxide. The theoretical research was encouraged considering the molecular description of ZnO as crystal solid using the density functional theory. The energy loss calculations for H and He ions with different charge states were performed with the shelwise local plasma approximation (SLPA). The molecular versus the Bragg-rule description is also discussed. The equilibrium charge state of He inside ZnO is analyzed based on the present stopping measurements, and a semiempirical charge state distribution is proposed. Present experimental and theoretical values show good agreement for both the stopping and the straggling. We also compare our data with the SRIM2013 and with CasP5.2 values.

## 1 Introduction

In recent years, the wide gap semiconductors, including ZnO, GaN and SiC, are revolutionizing numerous areas of developments due to their application in energy-efficient and environmentally friendly devices, from UV/blue light-emitting diodes (LED), sensors, photodetectors, to laser diodes, energy conversion, photovoltaics, communications, biotechnology, imaging, and medicine [1]. Currently the interest, especially in ZnO, is mainly due to the industrial demand. Some compounds based on ZnO are considered as promising fast scintillators [2], with a high radiation hardness and appropriate stopping power. For example, the ZnO:Zn scintillators containing Li have been developed for high-counting rate neutron imaging (see [1] and references therein). The aluminum doped ZnO on polymer foil is also applied in organic solar cell devices [3].

The interest in ZnO is not only based on its new technological applications, but also on the fact that ZnO has been a common material produced commercially at rather low cost for more than a century. Zinc oxide is available mostly in powder or thin film form and only recently a small single crystal ZnO has been produced [4]. In the wurtzite crystallize structure, ZnO is a direct band gap semiconductor with a band gap of 3.44 eV [5]. In a very recent letter [6] an all-optical experimental technique is presented and applied on a ZnO crystal to reconstruct the momentum-dependent band gaps.

Despite the extensive research described above, some basic properties of this material have not been established so far. Among them are the stopping power and straggling of light ions in the keV-MeV energy range. In turn these quantities are fundamental for the interpretation of the Rutherford Backscattering (RBS) results, which is one of the most used techniques for the thin film analysis. Moreover, it should be stated that no measurement on ZnO target is present in the exhaustive collection of stopping data by Paul [7] and Paul and Schinner [8]. Therefore, in this contribution we report the first set of experimental data of energy loss of H and He in ZnO, including stopping power and straggling.

The present data was measured using the RBS technique at the facility of the Instituto de Física, at the Universidade Federal do Rio Grande do Sul, Brazil. This research contributes to the study of the energy loss of ions in different oxides of interest, such as the widely measured $Al_2O_3$ [9,10], but also $HfO_2$ [11,12], $ZrO_2$ [13,14], $TiO_2$ [15] and $Ta_2O_5$ [16], for which no previous experimental data were available in the literature.

[a] e-mail: mclaudia@iafe.uba.ar

The theoretical description of the energy loss in complex targets is scarce. The MELF-GOS model is an interesting possibility if reliable measurements of the energy loss function in the optical limit are available [10–16]. In relation to the atomic values, in 1905 Bragg and Kleeman [17] predicted that the stopping power of a compound should be given by the linear combination of the different constituents. This well-known Bragg additivity rule is still employed, not only for stopping power, but also for ionization cross sections, considering the single atomic elements or the small molecular fragments of large molecules such as the nucleobases [18]. Deviations at intermediate and low energies occur mainly because of differences in the electronic structure of the outer shells, where molecular bonds start to become important [19]. A step forward is the core-and-bond approximation (CAB), where the core and outer electron contributions are separately considered [20]. The CAB approximation together with the stopping power data on an important amount of compounds is considered in the SRIM code to deal with stopping in compounds [21,22].

In this work we face the theoretical challenge of performing ab-initio stopping power calculations using the full molecular description of the ZnO in the solid phase. We use the shellwise local plasma approximation (SLPA) [23–25] together with the density functional theory (DFT) for the ZnO molecules as crystalline solid. This procedure has already been applied successfully in a previous work for $TiO_2$ target [15].

The SLPA is a many electron model that can be adapted perfectly to complex targets. Its inputs are the electronic densities and binding energies, so as far as a reliable molecular description of the ground state is available, the combination with the SLPA is straightforward. It should also be mentioned that the SLPA deals with atoms or molecules with the same degree of computational effort.

This paper is organized as follows. First, in Sections 2 and 3 we describe the experimental techniques for the sample preparation, the RBS measurements and the data analysis. Details about the SLPA and the DFT calculations are given in Section 4. Afterwards, in Section 5 the present experimental data and the theoretical results for stopping and straggling of H and He in ZnO are presented and discussed, including an empirical estimation of the equilibrium charge state of He inside the ZnO. Finally, the conclusions are summarized in Section 6.

## 2 Sample preparation and characterization

ZnO films were grown by Atomic Layer deposition (ALD) at the Institute of Physics, Polish Academy of Science, Warsaw. The growth processes were performed using the Savannah-100 reactor from Cambridge NanoTech. Diethylzinc (DEZn) as a zinc precursor and deionized water (DW) as an oxygen precursor were used, while nitrogen was applied as the purging gas. All films were grown at a constant growth rate of 0.07 nm/cycle.

Extensive sample characterization is essential for reliable stopping power measurements. In a large number of experiments performed to the date polycrystalline samples were used. This requires thorough analysis of crystallite size and their mutual orientation. It should be mentioned that the rolling texture, typically present in metallic foils, has been a source of important systematic errors in a number of stopping power measurements.

Structural characterization was performed using X-ray diffraction and AFM analysis. XRD measurements were performed at the Institute of Electronic Materials Technology, Warsaw, using the Siemens D500 powder diffractometer, equipped with a high-resolution semiconductor Si:Li detector and using $K_{\alpha 12}Cu$ radiation ($\lambda = 1.5418$ Å). The diffraction pattern was measured in a $(\theta - 2°)/2\theta$ scanning mode, with a step of 0.05°, counting time of 4 s/step and $2\theta$ range 25°–65°. The deviation of the specimen surface with two degrees of Bragg-Brentano geometry was done in order to attenuate strong reflections from the single crystal substrate. The experimental data were analyzed by the XRAYAN phase analysis program and ICDD PDF4+ 2013 database package of diffraction standards.

X-ray diffraction profiles revealed the presence of the Si 004 reflection due to the scattering by the substrate and three orders of magnitude lower ZnO 00.2 reflexion. The presence of the latter indicates that the films are of polycrystalline structure. The average crystallite size of about 25 nm has been estimated. This means the produced layers are nanocrystalline and what is very important no texture has been detected. Very low background level in diffraction profiles indicates negligible contribution of the amorphous phase. The results of the present experiments give place to the following thickness of films: $t = 22$, 44, 66, 104, 113 and 172 nm. The typical errors are less than 5%.

AFM measurements revealed that all the films are atomically flat with the Root Mean Square (RMS) of the surface roughness varied between 0.8 nm for the thinnest film (22 nm) to 1.6 nm for the thickest one (172 nm). These results are crucial for the straggling measurements. The detailed description of sample analysis can be found elsewhere [26]. The stoichiometry of the films were checked and confirmed by using the RBS spectrometry.

## 3 RBS measurements

### 3.1 Stopping power

The energy losses of H and He were determined by means of the RBS technique using the ions beams provided by the 3 MV Tandetron of the Instituto de Fisica, Universidade Federal do Rio Grande do Sul. For the H and He beams, the interval of energy covered by the present experiment was between 300 and 3000 keV and the combined electronic plus detector resolution were of 8 and 12 keV (FWHM) respectively. The samples were mounted on a goniometer and the detector was fixed at 120° with respect to the beam direction. For each incident energy, the angle between the beam and the normal to the sample was changed between 0° and 60°. The selection of the sample

thicknesses was done according to the beam energy. In some cases two different samples were analyzed with the same energy and the results were quite consistent with each other.

The stopping power $dE/dx$ can be obtained from the experimental data for the ions backscattered at a depth $x$ of the film, through the following relation based on the mean energy approximation [27]

$$\Delta E(x) = \frac{K\ x}{\cos\theta_1}\left.\frac{dE}{dx}\right|_{\overline{E}_{in}} + \frac{x}{\cos\theta_2}\left.\frac{dE}{dx}\right|_{\overline{E}_{out}}, \qquad (1)$$

where $\Delta E$ is the difference between the beam energy at the surface ($E_0$) and at the depth $x$, $K$ is the kinematic factor, $\theta_1$ ($\theta_2$) is the angle between the sample normal and the incoming beam (the detector direction), and $dE/dx|_{\overline{E}_j}$ is the stopping power at the energy $\overline{E}_j$.

Considering (1) for ions backscattered at the back of the ZnO film, $x$ equals the film thickness $\Delta x$. When measuring $\Delta E$ (the difference between $E_0$ and the energy at the back signal edge) at two or more different geometries, a system of equations is obtained which allows to get the stopping values $dE/dx|_{\overline{E}_{in}}$ and $dE/dx|_{\overline{E}_{out}}$. For each energy, four measurements were taken under different geometrical conditions ($\theta_1 =$ 0°, 20°, 40° and 60° and $\theta_2 = 60° - \theta_1$). The energies $\overline{E}_{in}$ and $\overline{E}_{out}$ were taken as the mean values of the values obtained via mean energy approximation [27]. Proceeding in the same way for each energy, the stopping powers of ZnO for H and He were obtained. See reference [12] for further details.

### 3.2 Straggling

The ion beams were provided by the 3 MV Tandetron, with incident energies covering a wide range. For H ions it was from 300 up to 1500 keV, while for He ions it was from 300 up to 3000 keV. For each incident beam and energy we have used an appropriate film. In each case we have recorded three spectra at 0°, 30° and 45° between the normal of the sample and the incident ion beam. This procedure was followed in order to improve the present results precision.

In Figure 1 we show a 1 MeV RBS signal of Zn belonging to a 172 nm ZnO film tilted at 30° with respect to the sample normal. The fits to the Zn signal are displayed with full lines. Following the procedure related in [11] and taking into account the RMS natural roughness we were able to obtain the straggling corresponding to each measured sample and measured energy.

## 4 Theoretical model

Our theoretical developments lay over two complementary models, the SLPA for the energy loss [23–25] (briefly summarized in Sect. 4.1) and the DFT applied to describe the ZnO in the crystaline solid face (described in Sect. 4.2).

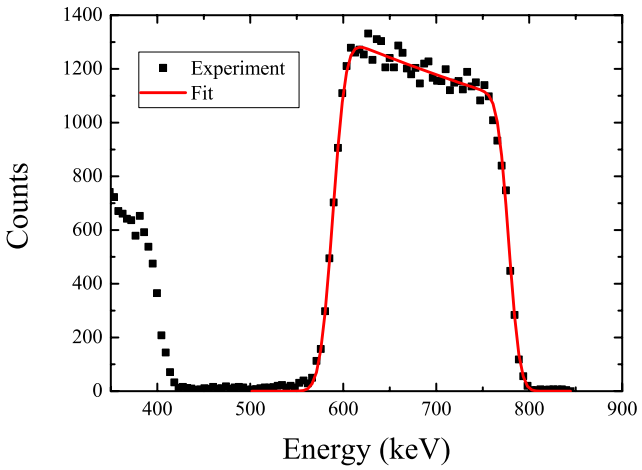


**Fig. 1.** RBS spectrum for 1 MeV He in ZnO. The symbols stand for the experimental spectrum. The line is a fit to the ZnO signal.

### 4.1 SLPA for the energy loss

We modeled the inelastic processes that take place when H or He ions interact with the ZnO electrons by using the SLPA [23]. This approximation works within the dielectric formalism describing the response of the bound electrons as a local electron gas with an ionization gap using Levine-Louie dielectric function for each subshell [28]. The SLPA is not an independent particle approximation, it includes single and collective processes, the dynamic screening of the projectile charge, and the electron correlation in the final state. The main limitation is that it is a perturbative formalism, valid for asymmetric collisions and high energies, i.e. $Z_P < Z_T$, and $Z_P/v < 1$, with $Z_P$ ($Z_T$) being the projectile (target) nuclear charge and $v$ the impact velocity. In addition, it is an impulse type approximation [29] and assumes that the time of response of target electrons is larger than the collision time, i.e. the ion impact velocity larger than the mean velocity of the bound electrons. Within this frame, the SLPA probed to describe the different energy loss moments, such as the ionization cross sections [30–33], the stopping power [24,25,34] and the energy loss straggling [35,36], in good agreement with the measurements.

Considering the inelastic collisions of the ion and the cloud of target electrons with binding energy $E_{nl}$ and local density $\rho_{nl}(\mathbf{r})$, the SLPA expression for the energy loss moment of order $t$ ($t = 0$ for the ionization cross section, $t = 1$ for the stopping power, $t = 2$ for the square energy loss straggling) is given by

$$S_{nl}^{(t)} = \frac{2}{\pi v^2}\int_0^\infty \frac{[Z_P(k)]^2}{k}dk \int_0^{kv} \omega^t Im\left[\frac{-1}{\varepsilon_{nl}(k,\omega)}\right] d\omega, \qquad (2)$$

with

$$\mathrm{Im}\left[\frac{-1}{\varepsilon_{nl}(k,\omega)}\right] = \int \mathrm{Im}\left[\frac{-1}{\varepsilon^{LL}(k,\omega,\rho_{nl}(\mathbf{r}),E_{nl})}\right] d\mathbf{r}, \qquad (3)$$

and with $\varepsilon^{LL}(k,\omega,\rho_{nl},E_{nl})$ being the Levine-Louie dielectric function [28]. The importance of using this dielectric function is the explicit inclusion of the binding energies. The total energy loss moment will be the addition of the shell to shell contributions, $S^{(t)}=\sum_{nl}S^{(t)}_{nl}$. More details about the SLPA can be found in [37], and a review on this approximation in [23].

We include the ion charge state in (2) as $Z_P(k)$ to take into account the dressed ions (i.e. $He^0$ and $He^+$) and the screened nuclear charge. Note that this is not a constant effective charge. It is calculated considering the wave functions of the ion bound electrons using Hartree-Fock tables for neutral and for positive ions by Clementti and Roetti [38], and transformed to the momentum space. For bare ions it is just $Z_P$. An analytical fitting of the exact values for ions $He^{+q}$ to $Ne^{+q}$ can be found in [23] together with tables for the different ions.

When the ion travels inside the solid, ionization and capture processes take place leading to an equilibrium charge state, which depends on the ion velocity. At high energies, electron loss prevails over capture and the ion ends stripped from bound electrons. We performed the SLPA calculations for the different possible equilibrium charge states of the ion by using (2) and (3). In this equilibrium regime (many collisions inside the bulk), the total stopping can be approximated as

$$S^{(t)}_{total}=\sum_{q=0}^{Z_P}f_q(v)S^{(t)}, \tag{4}$$

with $f_q(v)$ being the charge fraction of $H^{+q}$ $(q=0,1)$ or $He^{+q}$ $(q=0,1,2)$. The mean charge state is $q_{mean}(v)=\sum_q q\ f_q(v)$.

Total stopping power calculations are very sensitive to these values. In some cases experimental values are available. Well-known fittings of the experimental mean charge states are those by Grande and Schiwietz [39,40], and by Ziegler et al. [41] (included in the SRIM code [21,22]). Both proposals, while different, show good descriptions of the stopping cross sections tested on an extended ion-target sampling. However, measurements of equilibrium charge states for the different projectile-target combinations, including compounds, are still necessary. Particularly, there are no experimental values on Zn or ZnO. Experimental and theoretical works are still focused on this subject [42–47] due to the relevance of reliable values of the charge state distributions of ions through matter. We will return to this point in Section 5.2.

### 4.2 DFT for ZnO

We resort to the density functional theory (DFT) to obtain the ZnO electronic density, the binding energies, the cohesive energy, and the band structure. The radial wave functions of the core electrons, the pseudopotentials and the pseudo-atomic orbitals of the valence electrons were generated by means of the ADPACK and OpenMX codes. These codes solve numerically the non-relativistic Kohn-Sham equations under the generalized gradient approximation (GGA) with a Troullier and Martins scheme [48], and following the developments of Perdew, Burke and Ernzerhof [49], also known as GGA-PBE. The calculations were carried out for the $Zn^{2+}$-$O^{2-}$ configuration, i.e. the valence band O-2$p$ completely filled. A similar procedure was introduced in [15] for $TiO_2$.

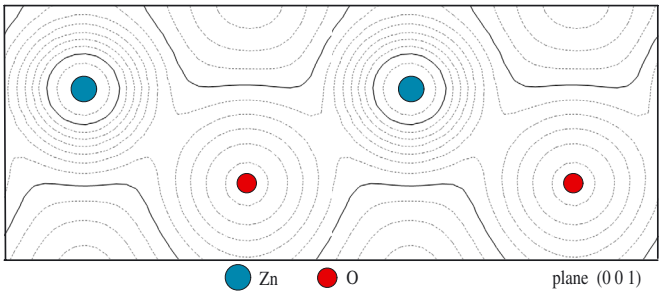


**Fig. 2.** The wurtzite crystal structure electron density.

We assumed ZnO to be hexagonal zincite in space group 186 with Hermann Mauguin notation P63/mc [50] (see Fig. 2). The lattice constants were determined by energy minimization per molecule. We obtained $a=3.29$ Å and $c=5.40$ Å, very close to the experimental values $a=3.2495$ Å and $c=5.2069$ Å [50]. We also calculate the cohesive energy of ZnO, –6.85 eV, while the experimental one is –7.52 eV (deduced from experimental Zn heat vaporization, ZnO enthalpy of formation, and O2 binding energy for the wurtzite phase [51]). Some authors [52] consider that the DFT-GGA severely underestimates the gap. This is not the case for present calculations. We obtain a band-gap of 3.65 eV, where experimental value is 3.44 eV at low temperatures and 3.37 eV at room temperature [53,54]. This value is rather good, though 7% above the experimental value. Present results for the band structure of ZnO using DFT-GGA-PBE calculations are displayed in Figure 3.

The binding energies of the target electrons are important inputs for the SLPA calculations. Present DFT-GGA results for the ZnO valence electrons (in atomic units) are $E_{2p}=-0.355$ a.u. for the $O^{2-}$ and $E_{3d}=-0.395$ a.u. for the $Zn^{2+}$. These energies are around half of the corresponding atomic ones ($E_{2p}=-0.632$ a.u. and $E_{3d}=-0.783$ a.u. [38]). This is interesting because the SLPA describes the response of the ZnO valence shell as separate clouds of the six O-2$p$ electrons and the ten Zn-3$d$ electrons, with rather similar binding energies and mean velocity around 0.9 a.u. The contribution of these subshells is very important at the energies of the stopping maximum. We will return on this point in Section 5.2.

The other input for the SLPA is the target electronic density. The quality of the DFT-GGA-PBE can be verified by comparing the calculated electronic density with the experiments of Compton scattering [55]. In a non-relativistic and high-energy transfer regime, theoretical calculations for isotropic Compton profiles are commonly performed under the impulse approximation. It is

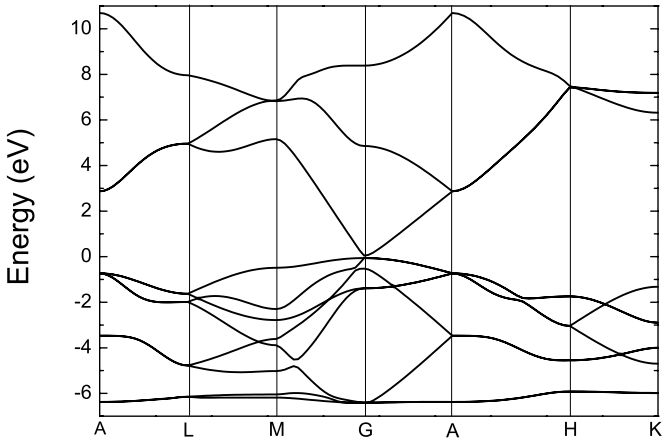


**Fig. 3.** Band structure calculation of ZnO using GGA-PBE functional.

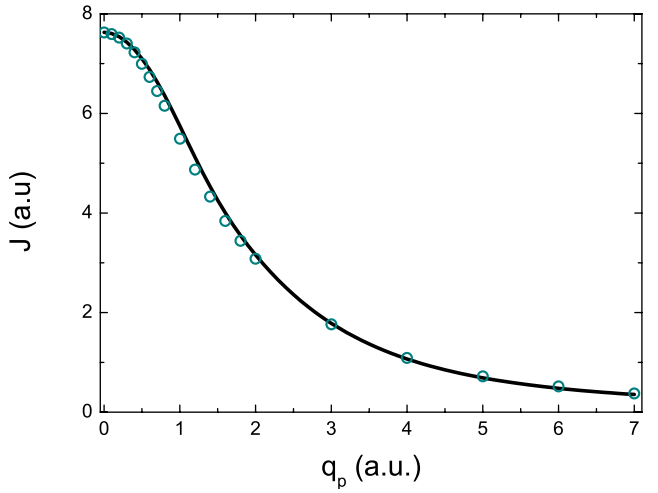


**Fig. 4.** Compton profile of ZnO. The solid curve indicates the present DFT-GGA calculation, whereas the circles are the experimental data from reference [55].

assumed that energy and momentum are conserved. This approach is expected to be valid when the energy transferred in the scattering process is much greater than the binding energy of the electron orbital [56].

The isotropic Compton profile (in atomic units) under the impulse approximation, is defined as:

$$J(q_p) = \frac{1}{2}\int_{q_p}^{\infty} n(p)\, p\, dp, \qquad (5)$$

where $n(p)$ is electron momentum density related to the square of the Fourier transform of the radial wave function, $p$ is the electron linear momentum before the collision (in module), and $q_p$ is the projection of the momentum transfer on the direction of $\overrightarrow{p}$.

Present DFT-GGA-PBE results for the Compton profile of crystaline ZnO are compared with Kumar et al. [55] measurements in Figure 4, showing a very good description of the data. This method has already been tested for $TiO_2$ [15] with very good agreement too, as noted in reference [57].

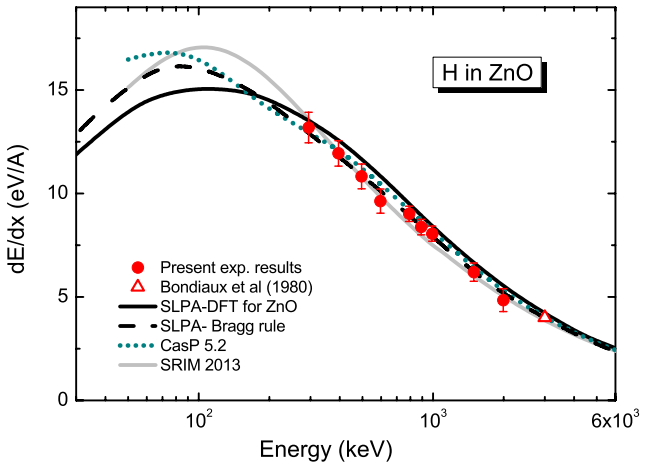


**Fig. 5.** Stopping power of ZnO for protons. Symbols: filled circles, present data; hollow triangle, [58]. Curves: solid line, present SLPA calculations with DFT molecular values for ZnO; dashed-line, SLPA for ZnO using Bragg rule (atomic Zn and O); dotted-line Casp5.2 values [39,40,59–61]; grey-solid line, SRIM 2013 values [21,22].

## 5 Results and discussion

### 5.1 Stopping and straggling of ZnO for H

In Figure 5 we display the present experimental data (filled squares) and the theoretical values (solid curve) for the mean energy loss per unit path length, $dE/dx$, of H in ZnO bulk. The stopping per unit path length given by (4) relates to the stopping cross section per molecule as $S^{(1)}\rho = dE/dx$. In the present case, the density of ZnO molecules is $\rho = 4.148 \times 10^{22}$ molecules/cm$^3$.

There is only one previous value available in the literature for stopping of H by ZnO by Blondiaux et al. [58], at 3 MeV, which is also displayed in Figure 5. The tendency of the present data is in agreement with this value. The SLPA results shown in Figure 5 have been obtained using the DFT-GGA molecular values for ZnO as described in Section 4.1.

For impact energies $E \geq 300$ keV, the equilibrium charge state of H is +1, so in the energy range of present experimental data the description of the $H^+$-ZnO collision is enough. Following [39,40], the extension of present SLPA results to energies below 200 keV should consider the presence of $H^0$ inside ZnO. In that case, the total stopping of H in ZnO for $E < 200$ keV would be lower than the results shown in Figure 5.

We also include in Figure 5 the SLPA calculations using Bragg rule (adding the atomic results for Zn and O), the predictions of the convolution approximation for swift particles (CasP5.2) [59–61], and the semi-empirical SRIM2013 values [21,22]. It is worth to mention that

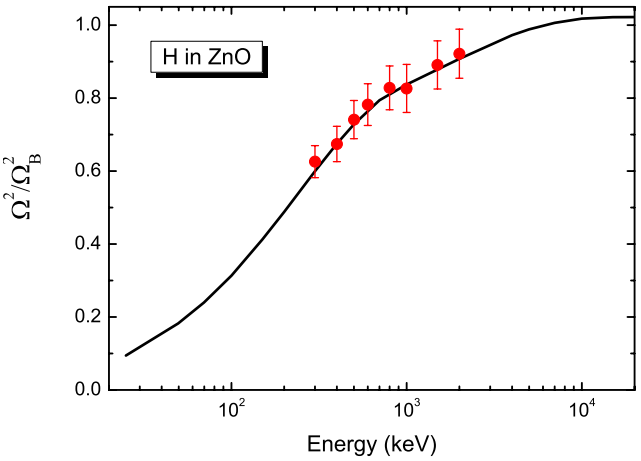


**Fig. 6.** Square energy loss straggling of H ions in ZnO, normalized to Born value. Symbols: filled circles, present data. Curves: solid line, present SLPA calculations with DFT molecular values for ZnO.

SRIM values for H in solids only consider the +1 charge state.

Our full-molecular SLPA-DFT results in Figure 5 (solid-line) correctly describe the present experimental values. It is fair to say that also the atomic SLPA results using the Bragg rule (dashed-line) agree quite well with the high energy measurements. The different predictions for the stopping of H in ZnO included in Figure 5 describe the data for $E \geq 300$ keV/amu and differ for lower energies. The differences around the stopping maximum cannot be solved without measurements in this energy region. The SLPA probed to be valid for energies somewhat lower than the stopping maximum [23]. But it is a perturbative approximation, to lower energies the Barkas effect should be estimated [46], or a non-perturbative model should be used.

In Figure 6 we display present experimental and theoretical values for the square energy loss straggling per molecule, $\Omega^2 = S^{(2)}_{total}$ given by (4). These values are normalized to Bohr high energy limit $\Omega^2_B = 4\pi\, Z_P^2\, Z_T \rho\, \Delta x$ [62], with $\rho$ being the target density and $\Delta x$ being the width. The agreement is quite good in the whole experimental energy range. Straggling measurements represent a highly demanding test of the sample preparation described in Section 2.

### 5.2 Stopping and straggling of ZnO for He

We performed the SLPA calculations for $He^0$, $He^+$, and $He^{+2}$ using (2) with the corresponding screening functions $Z_P(k)$. In the equilibrium regime the total stopping is obtained considering the ion charge state at each impact velocity as expressed in (4). Present stopping measurements suggest that the charge state of He in ZnO is close to +2, even at 400 keV/amu. This value is greater than CasP code prediction based on the fitting in [39,40] for atomic targets and Bragg rule [17].

The charge state of fast ions moving through matter fluctuates due to electron loss and capture processes. After a large number of collisions, an equilibrium charge state is reached, which is independent of the ion incident charge state, it only depends on the impact energy and the target. This subject has been extensively studied for ions through gaseous and solid media. Reviews on this can be found in [63] and more recently in [64].

A benchmark for the equilibrium charge state is the known Thomas-Fermi (TF) charge, based on Bohr stripping criteria [47]

$$q_{eq} = Z_P[1 - \exp(-v/Z_P^{2/3})]. \tag{6}$$

More complex theoretical developments are based on TF function [65]. An analytical fitting formula based on this model has been recently given by Sigmund [64] as

$$q_{eq} = Z_P\, \frac{1 - \exp(-1.43\ v/Z_P^{2/3})}{1 + \exp(-3.56\ v/Z_P^{2/3})}. \tag{7}$$

Empirical fittings for specific ion-target combinations are also available in the literature, [66–68], including a recent two-parameter fitting for heavy ions in different targets by Sagaidak et al. [45]. Of course, all the different ion-target systems cannot be covered. Betz proposal [66] is to fit the measured equilibrium charge as

$$q_{eq} = Z_P\ [1 - \alpha\ \exp(-v/Z_P^{\gamma})], \tag{8}$$

with $\alpha$ and $\gamma$ being fitting parameters for specific ion-target data. TF model predicts $\gamma = 2/3$, while for To and Drouin it is $\gamma = 0.45$ [67].

Perhaps the most accurate proposal of equilibrium charge state of ions in matter is that by Schiwietz and Grande [39,40], highly probed for different systems and used in stopping power calculations. It is based on a universal scaling (different projectiles and targets) ratified by an important amount of experimental data. This empirical scaling and fitting is employed in CasP code [39,40] and in many other stopping power calculations [15,24].

For compounds many of the semiempirical models use Bragg rule [17] despite the fact that for cases such as ZnO, it is a semiconductor with a clear band gap, while Zn is a metal, and the ratio between loss and capture cross sections is expected to be quite different. In previous calculations of stopping of He in oxides [15] we obtain the stopping cross sections using the values of the equilibrium charge fractions at each impact velocity supplied by the CasP code [39,40]. However, we found experimental evidence of $He^{2+}$ at lower energies than those predicted by [39,40]. In this contribution we estimate empirically the mean charge state of He inside ZnO as the square root of the ratio of the present He to H stopping measurements,

$$q_{eq} = \sqrt{S(\mathrm{He})/S(\mathrm{H})}. \tag{9}$$

This value is also called effective charge [41], and has been extensively used and discussed in stopping power calculations. At high energies the energy loss depends on the ion

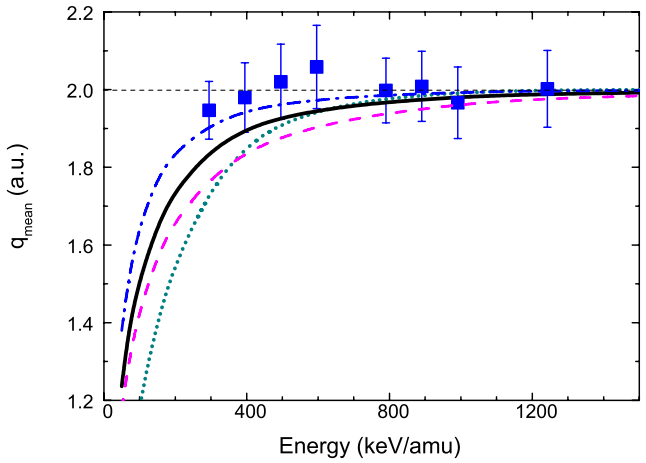


**Fig. 7.** Mean charged state of He inside ZnO. Symbols: filled squares, present data. Curves: solid line, present semiempirical proposal; dotted-line, Casp values [39,40]; dashed-line, standard TF expression in (6); dashed-dotted line, Sigmund formula given by (7) [64].

charge as $Z_P^2$ (perturbative regime). Lower values are expected for intermediate to low energies (saturation, non-perturbative regime, presence of $He^+$ ions). A review on the advantages and failures of the effective charge concept can be found in [47].

We decided to evaluate the charge state of He in ZnO by comparing our stopping measurements for He and H ions, and calculating the empirical $q_{eq}$ given by (9). In Figure 7 we display present experimental values for $q_{eq}$ at ion energies $E \geq 300$ keV/amu. The interesting point is that it is an insight on the charge state inside the solid. As expected, at high energies the measured $q_{eq}$ is close to the nuclear charge, and it is slightly below +2 for $(300 \leq E \leq 400)$ keV/amu. Based on these results we propose an empirical function for $q_{eq}(v)$ of He inside solid ZnO, also displayed in Figure 7 (solid line). This proposal considers the experimental values for energies $E \geq 400$ keV/amu, and extend it to lower energies. We take into account the experimental error in this fitting following the smallest value for $E \leq 600$ keV/amu. The criteria was to change the least possible from the universal scaling by Schiwietz and Grande in [39,40], also displayed in Figure 7. Our curve can be fitted by a Betz type function, given by (8), with $\gamma = 0.45$, as suggested by To and Drouin [67]. We also include in Figure 7 the results given by (6) and (7). Of course, the accuracy of TF theory is expected to be valid for ions with atomic number larger than 2, however, the agreement of Sigmund formula (7) with present measurements in this figure is amazing.

In Table 1 we present the numerical results of present empirical function for He in ZnO. The charge state fractions $f_q(v)$ were obtained considering that in the energy range of present experiments only $He^{+2}$ and $He^+$ can be found inside the ZnO. It can be noted that the difference with respect to [39,40] is only for energies below 500 keV/amu. We use the values in Table 1 to obtain the total stopping using (4).

**Table 1.** Equilibrium charge state of He in ZnO as function of the ion energy ($E$ in keV/amu). Charge fractions $f_q$ (in percentage) and equilibrium charge state $q_{eq}$ (in atomic units) correspond to the fitting in Figure 7. The $q_{eq}^{\rm exp}$ are obtained from the ratio of our stopping measurements as in (9). Also included are the CasP values [39,40], $q_{eq}^{\rm CasP}$.

| $E$ | $f_0$ | $f_1$ | $f_2$ | $q_{eq}$ | $q_{eq}^{\rm exp}$ | $q_{eq}^{\rm CasP}$ |
|---|---|---|---|---|---|---|
| 30 | 15.0 | 72.5 | 12.5 | 0.97 | | 0.611 |
| 50 | 3.9 | 68.6 | 27.5 | 1.24 | | 0.828 |
| 100 | 0.0 | 48.9 | 51.1 | 1.51 | | 1.19 |
| 200 | 0.0 | 25.8 | 74.2 | 1.74 | | 1.56 |
| 300 | 0.0 | 15.5 | 85.5 | 1.84 | 1.95 ± 0.07 | 1.75 |
| 400 | 0.0 | 10.1 | 89.9 | 1.90 | 1.98 ± 0.09 | 1.86 |
| 500 | 0.0 | 7.0 | 93.0 | 1.93 | 2.02 ± 0.10 | 1.92 |
| 600 | 0.0 | 5.2 | 94.8 | 1.95 | 2.06 ± 0.10 | 1.95 |
| 800 | 0.0 | 2.9 | 97.1 | 1.97 | 2.00 ± 0.08 | 1.98 |
| 900 | 0.0 | 2.3 | 97.7 | 1.98 | 2.01 ± 0.09 | 1.99 |
| 1000 | 0.0 | 1.8 | 98.2 | 1.98 | 1.97 ± 0.09 | 1.99 |
| 1250 | 0.0 | 1.2 | 98.8 | 1.98 | 2.00 ± 0.10 | 2.00 |
| 1500 | 0.0 | 0.7 | 99.3 | 1.99 | | 2.00 |
| 2000 | 0.0 | 0.4 | 99.6 | 2.00 | | 2.00 |
| 5000 | 0.0 | 0.0 | 100 | 2.00 | | 2.00 |

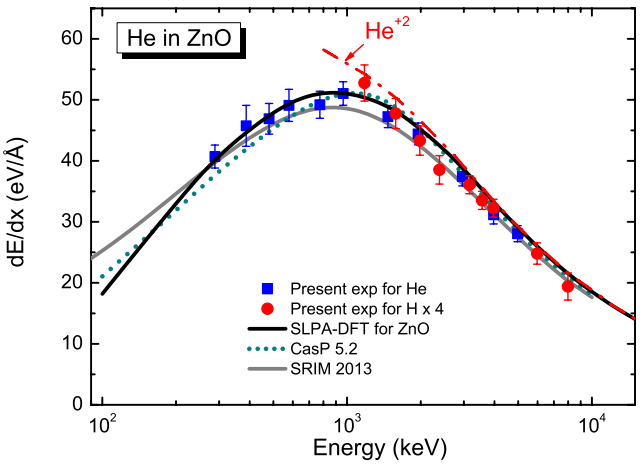


**Fig. 8.** Stopping power of ZnO for He ions. Symbols: filled squares, present measurements for He ions; filled circles, present data for H ions $\times Z_P^2$. Curves: solid line, present SLPA calculations with DFT molecular values for ZnO; dotted-line Casp5.2 values [39,40,59–61]; grey-solid line, SRIM 2013 values [21,22].

In Figure 8 we display our experimental data and theoretical results for the stopping power per unit path length of He ions in ZnO. The molecular SLPA calculations for ZnO were performed considering the different He ions ($He^0$, $He^+$ and $He^{+2}$), and the $f_q$ values displayed in Table 1. Present measurements for He in ZnO cover the stopping maximum. The SLPA results show good agreement with the experimental measurements in the extended (0.3–10) MeV energy region. We also display in this figure the present measurements for H in ZnO × 4. The experimental agreement among He and H × $Z_P^2$ measurements above 1400 keV is clear, indicating that Barkas contribution

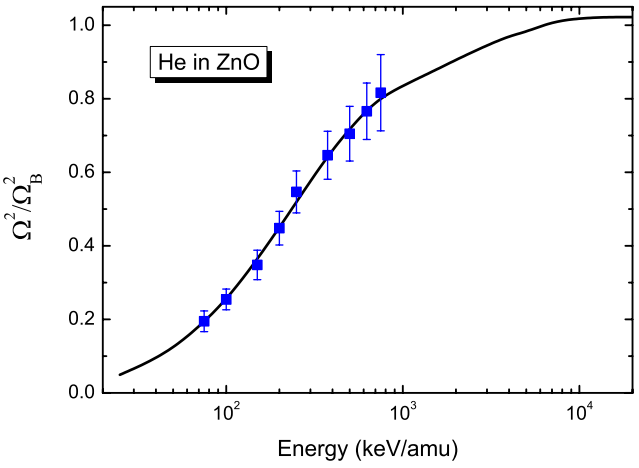


**Fig. 9.** Square energy loss straggling of He ions in ZnO, normalized to the Born value. Symbols: filled squares, present data. Curves: solid line, present SLPA calculations with DFT molecular values for ZnO; grey dashed dotted-line, similar calculation only for $He^{+2}$ ions.

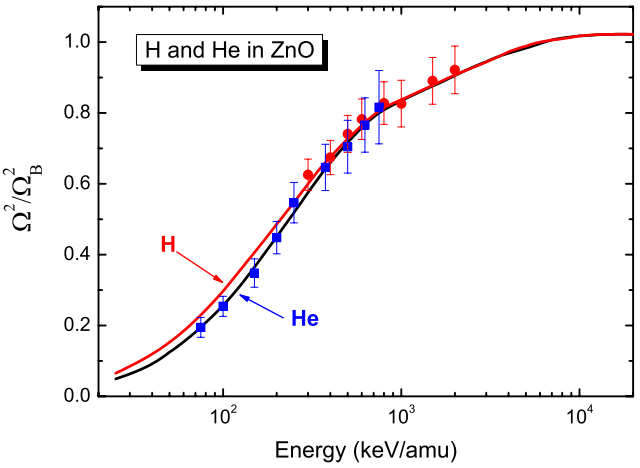


**Fig. 10.** Square energy loss straggling of H and He in ZnO, normalized to the Born value. Symbols: grey hollow-squares, present data for H ions, black filled-squares, present data for He ions. Curves: black solid line, present SLPA-DFT values for He in ZnO; grey solid-line present SLPA-DFT calculations for H in ZnO.

($Z^3$ dependence) is negligible in this region. These data also agree quite well with the SLPA results for $He^{+2}$ shown in Figure 8. The difference between this $He^{+2}$ curve and the total one is due to the $He^{+1}$ and $He^0$ ions at intermediate and low energies.

Also in Figure 8 are the predictions by the CasP5.2 code [39,40,59–61] (binary collisional model, includes Barkas contribution) and by the SRIM2013 algorithm [21, 22]. The different descriptions agree rather well with the new data, with the SRIM values being somewhat low, but within the experimental error. The SLPA and the CasP5.2 curves are together above 1 MeV, below 600 keV the SLPA shows a better description of the experimental data. In this energy region the response of the valence electrons is decisive. We found that the ZnO outer electrons ($2p$ of $O^{-2}$ and $3d$ of $Zn^{+2}$) are the main contribution to the stopping power for He impact energies up to 2 MeV. This covers the stopping maximum, reinforcing the DFT description of the ZnO molecule and its binding energies, as mentioned in Section 4.2. The SLPA-experimental agreement displayed in Figure 8 is quite good down to 300 keV, feature that can be assigned to the collective character of the theoretical treatment. The presence of dressed ions ($He^0$ and $He^+$) and the dynamic screening of the ion by the target electrons (collective response) reduce the effective potential and expand the validity of our perturbative approach. For lower energies, the contributions of higher perturbative orders such as the Barkas-Andersen effect are important. However, this effect is not straightforwardly quantified for dressed ions [46].

Present measurements and calculations for the square energy loss straggling are displayed in Figure 9. The full SLPA calculation, considering the charge states of He in ZnO given in Table 1, is in very good agreement with the present data. This is a second test for our proposal.

The square energy loss straggling normalized to Bohr ($\Omega_B^2 \; \alpha \; Z_P^2$) is almost insensitive to the ion charge (at least for low charged ions and intermediate to high energies). In Figure 10 we plotted together the experimental and theoretical values for the energy loss straggling in ZnO for H and He ions. We can note that the measurements for H and He in ZnO are quite close above 300 keV/amu. This is the expected behavior and reinforces present measurements of the energy loss straggling.

## 6 Conclusions

In this work we present a theoretical-experimental study of the stopping and straggling of H and He ions into ZnO matrix. The theoretical approach is based on the SLPA formalism, with DFT to describe the ZnO crystal; while the experiments were realized using the RBS technique. The theoretical-experimental agreement for the stopping power values is quite good. In the particular case of the He data, they reproduce very well the predicted maximum stopping power, feature that is not easy to achieve. It would be worthwhile to mention that the theoretical results are in general very sensitive to the charge state of the ions inside the matrix. In the present case we have considered $H^+$ for the H ions in view of their high velocity inside the ZnO sample. This is not the case for He where $He^0$, $He^+$ and $He^{+2}$ contribute to the stopping power. We give a semiempirical proposal for the charge states of He inside ZnO bulk based on present measurements of the stopping power. Down to 500 keV the present and the CASP predictions concerning the mean charge agree, however for lower energies there is a small difference, which strongly reflects on the stopping power results. At variance, the straggling results are not too much sensitive to the charge state. The theoretical-experimental agreement for the energy loss straggling is very good for both, H and He impact.

In memory of Helmut Paul, whose scientific contributions and compilation of data on stopping power have been of great importance to our community. The authors thank Prof. Jorge Miraglia for useful comments. The following institutions financially support this research: in Brazil the CNPq by the contract PDJ 500314 2014/4; in Argentina, the CONICET by the PIP2014-2016, the ANPCyT PICT 2014-2363, and the University of Buenos Aires by the projects UBACyT 20020130100 632BA and 20020130100 477BA.

## References

1. *Handbook of Zinc Oxide and Related Materials*, edited by Z.C. Feng (CRC Press, Taylor and Francis Group), Vol. II, pp. 435-484
2. V.A. Demidenko E.I. Gorokhova, I.V. Khodyuk, O.A. Khristich, S.B. Mikhrin, P.A. Rodnyi, Radiat. Meas. **42**, 549 (2007)
3. M. Dosmailov, L.N. Leonat, J. Patek, D. Roth, P. Bauer, M.C. Scharber, N.S. Sariciftci, J.D. Pedarniga, Thin Solid Films **591**, 97104 (2015)
4. P.J. Simpson, R. Tjossem, A.W. Hunt, K.G. Lynn, V. Munné, Nucl. Instrum. Meth. Phys. Res. A **505**, 82 (2003)
5. H. Morkoc, U. Özgür, *Zinc Oxide, Fundamental, Materials and Device Technology* (Wiley-VCH Verlag GmbH&Co KGaA, Weinheim, 2009), Chap. 1
6. G. Vampa, T.J. Hammond, N. Thiré, B.E. Schmidt, F. Légaré, C.R. McDonald, T. Brabec, D.D. Klug, P.B. Corkum, Phys. Rev. Lett. **115**, 193603 (2015)
7. H. Paul, *Stopping Power for Light Ions*. https://www-nds.iaea.org/stopping/
8. H. Paul, A. Schinner, Nucl. Instrum. Meth. Phys. Res. B **227**, 461 (2005)
9. E.D. Cantero et al., Nucl. Instrum. Meth. Phys. Res. B **287**, 1 (2012)
10. M. Behar, R.C. Fadanelli, L.C.C.M. Nagamine, E.D. Cantero, G.H. Lantschner, J.C. Eckardt, N.R. Arista, C.D. Nascimento, R. Garcia-Molina, I. Abril, Eur. Phys. J. D **68**, 194 (2014)
11. I. Abril, M. Behar, R. Garcia-Molina, R.C. Fadanelli, L.C.C.M. Nagamine, P.L. Grande, L. Schünemann, C.D. Denton, N.R. Arista, E.B. Saitovitch, Eur. Phys. J. D **54**, 65 (2009)
12. M. Behar, R.C. Fadanelli, I. Abril, R. Garcia-Molina, C.D. Denton, L.C.C.M. Nagamine, N.R. Arista, Phys. Rev. A **80**, 062901 (2009)
13. M. Behar, R.C. Fadanelli, I. Abril, R. Garcia-Molina, L.C.C.M. Nagamine, Eur. Phys. J. D **64**, 297 (2011)
14. M. Behar, C.D. Denton, R.C. Fadanelli, I. Abril, E.D. Cantero, R. Garcia-Molina, L.C.C.M. Nagamine, Eur. Phys. J. D **59**, 209 (2010)
15. S.P. Limandri, R.C. Fadanelli, M. Behar, L.C.C.M. Nagamine, J.M. Fernández-Varea, I. Abril, R. Garcia-Molina, C.C. Montanari, J.C. Aguiar, D. Mitnik, J.E. Miraglia, N.R. Arista, Eur. Phys. J. D **68**, 194 (2014)
16. R.C. Fadanelli, M. Behar, L.C.C.M. Nagamine, M. Vos, N.R. Arista, C.D. Nascimento, R. Garcia-Molina, I. Abril, J. Phys. Chem. C **119**, 20561 (2015)
17. W.H. Bragg, R. Kleeman, Philos. Mag. **10**, 318 (1905)
18. S. Paredes, C. Illescas, L. Méndez, Eur. Phys. J. D **69**, 178 (2015)
19. L.N. Trujillo-López, C. Martínez-Flores, R. Cabrera-Trujillo, Nucl. Instrum. Meth. Phys. Res. B **313**, 5 (2013)
20. H. Paul, A. Schinner, Nucl. Instrum. Meth. Phys. Res. B **249**, 1 (2006)
21. J.F. Ziegler, J.M. Manoyan, Nucl. Instrum. Meth. Phys. Res. B **35**, 215 (1988)
22. J.F. Ziegler, J.M. Manoyan, SRIM code, http://www.srim.org/
23. C.C. Montanari, J.E. Miraglia, Theory of Heavy Ion Collision Physics in Hadron Therapy, in *Advances in Quantum Chemistry*, edited by Dz. Belkic (Elsevier, Amsterdam, 2013), Chap. 7, pp. 165-201.
24. E.D. Cantero, R.C. Fadanelli, C.C. Montanari, M. Behar, J.C. Eckardt, G.H. Lantschner, J.E. Miraglia, N.R. Arista, Phys. Rev. A **79**, 042904 (2009)
25. C.C. Montanari, C.D. Archubi, D.M. Mitnik, J.E. Miraglia, Phys. Rev. A **79**, 032903 (2009)
26. E. Guziewicz, A. Turos, A. Stonert, D. Snigurenko, B.S. Witkowski, R. Diduszko, M. Behar, Thin Solid Films **612**, 337 (2016)
27. W.K. Chu, J.W. Mayer, M.A. Nicolet, *Backscattering Spectrometry* (Academic, New York, 1978).
28. Z.H. Levine, S.G. Louie, Phys. Rev. B **25**, 6310 (1982)
29. J.D. Fuhr, V.H. Ponce, F.J. García de Abajo, P.M. Echenique, Phys. Rev. B **57**, 9329 (1998)
30. J.E. Miraglia, M.S. Gravielle, Phys. Rev. A **78**, 052705 (2008)
31. J.E. Miraglia, M.S. Gravielle, Phys. Rev. A **81**, 042709 (2010)
32. J.E. Miraglia, Phys. Rev. A **79**, 022708 (2009)
33. U. Kadhane, C.C. Montanari, L. Tribedi, J. Phys. B **36**, 3043 (2003)
34. C.C. Montanari, J.E. Miraglia, J. Phys. B **47**, 015201 (2014)
35. C.C. Montanari, J.E. Miraglia, AIP Conf. Proc. **1525**, 259 (2013)
36. C.C. Montanari, J.E. Miraglia, S. Heredia-Avalos, R. Garcia-Molina, I. Abril, Phys. Rev. A **75**, 022903 (2007)
37. C.C. Montanari, J.E. Miraglia, M. Behar, P.F. Duarte, N.R. Arista, J.C. Eckardt, G.H. Lantschner, Phys. Rev. A **77**, 042901 (2008)
38. E. Clementi, C. Roetti, At. Data Nucl. Data Tables **14**, 177 (1974)
39. G. Schiwietz, P.L. Grande, Nucl. Instrum. Meth. B **175-177**, 125 (2001)
40. G. Schiwietz, P.L. Grande, CasP code, available online in http://www.casp-program.org/
41. J.F. Ziegler, J.P. Biersack, U. Littmark, *The stopping and Range of ions in solids* (Pergamon Press, 1985)
42. C. Schmitt, J. LaVerne, D. Robertson, M. Bowers, W. Lu, P. Collon, Phys. Rev. A **80** 052711 (2009)
43. C. Schmitt, J. LaVerne, D. Robertson, M. Bowers, W. Lu, P. Collon, Nucl. Instrum. Meth. Phys. Res. B **268** 1551 (2010)
44. C. Schmitt, J. LaVerne, D. Robertson, M. Bowers, W. Lu, P. Collon, Nucl. Instrum. Meth. Phys. Res. B **269**, 721 (2011)
45. R.N. Sagaidak, V.K. Utyonkov, S.N. Dmitriev, Nucl. Instrum. Meth. B **365**, 447 (2015)
46. P. Sigmund, A. Schinner, Eur. Phys. J. D **68**, 318 (2014)
47. P. Sigmund, A. Schinner, Nucl. Instrum. Meth. Phys. Res. B (2016), in press, DOI:10.1016/j.nimb.2015.12.041
48. N. Troullier, J.L. Martins, Phys. Rev. B **43**, 1993 (1991)
49. J.P. Perdew, K. Burke, M. Ernzerhof, Phys. Rev. Lett. **77**, 3865 (1996)

50. *CRC Handbook of Chemistry and Physics*, edited by D.R. Lide, 89th edn. (CRC Press, Boca Raton, 2009)
51. H.K. Kim, S.H. Han, T.Y. Seong, W.K. Choi, J. Electrochem. Soc. **148**, G114 (2001)
52. A. Schleife, C. Rödl, F. Fuchs, J. Furthmüller, F. Bechstedt, Phys. Rev. B **80**, 035112 (2009)
53. A. Mang, K. Reimann, St. Rübenacke, Solid State Commun. **94**, 251 (1995)
54. V. Kumar, R.G. Singh, L.P. Purohit, F. Singh, Adv. Mat. Lett. **4**, 423 (2013)
55. R. Kumar, M.C. Mishra, B.K. Sharma, V. Vyas, G. Sharma, Electron. Mater. Lett. **9**, 19 (2013)
56. J.C. Aguiar, D. Mitnik, H.O. Di Rocco, J. Phys. Chem. Solids **83**, 64 (2015)
57. M. Vos, Nucl. Instrum. Meth. Phys. Res. B **366**, 6 (2016)
58. G. Blondiaux, M. Valladon, K. Ishii, J.L. Debrun, Nucl. Instrum. Meth. **168**, 29 (1980)
59. G. Schiwietz, P.L. Grande, Nucl. Instrum. Meth. Phys. Res. B **153**, 1 (1999)
60. G. Schiwietz, P.L. Grande, Nucl. Instrum. Meth. B **273**, 1 (2012)
61. G. Schiwietz, P.L. Grande, Phys. Rev. A **84**, 052703 (2011)
62. N. Bohr, Philos. Mag. **30**, 581 (1915)
63. A.F. Lifschitz, N.R. Arista, Phys. Rev. A **69**, 012902 (2004)
64. P. Sigmund, *Particle Penetration and Radiation Effects, Penetration of atomic and molecular ions* (Springer, Switzerland, 2014), Vol. 2
65. W.E. Lamb, Phys. Rev. **58**, 696 (1940)
66. H.D. Betz, Rev. Mod. Phys. **44**, 465 (1972)
67. K.X. To, R. Drouin, Nucl. Instrum. Meth. **160**, 461 (1978)
68. A. Itoh, H. Tsuchida, T. Majima, A. Yogo, A. Ogawa, Nucl. Instrum. Meth. Phys. Res. B **159**, 22 (1999)